Research Aircraft Measurements of Jet Stream Geostrophic and Ageostrophic Winds

M. A. SHAPIRO AND P. J. KENNEDY

National Center for Atmospheric Research,[1] P.O. Box 3000, Boulder, CO 80307

(Manuscript received 2 April 1981, in final form 6 July 1981)

ABSTRACT

Radar altimeter and inertial navigation wind velocity measurements from research aircraft are shown to give the ageostrophic wind velocity distribution within a jet stream system near the tropopause. Results from one case study reveal cross-height-contour ageostrophic winds exceeding 20 m s^{-1}, and centripetal-acceleration-induced ageostrophic winds approaching 100 m s^{-1} in the exit region of a jet streak which has entered into the trough region of a synoptic wave. Diagnostic calculations are made of the horizontal velocity divergence and the geostrophic and ageostrophic components of the observed wind velocity acceleration. The results suggest caution in the application of near-straight jet-streak dynamics and the geostrophic momentum approximation to jet-streak systems embedded within large-amplitude synoptic wave regimes.

1. Introduction

The implementation of the synoptic upper air network during the 1930's and 1940's provided meteorologists with their first views of the three-dimensional distribution of wind velocity and temperature within extratropical cyclones and their associated jet streams and frontal zones. These observations revealed that, to the first order of approximation, the horizontal velocity $\mathbf{V}$ is in geostrophic balance with the geopotential gradient $\nabla\Phi$

$$\frac{d\mathbf{V}}{dt} \ll f\hat{k} \times \mathbf{V} \approx -\nabla\Phi = f\hat{k} \times \mathbf{V}_g, \qquad (1)$$

where $\mathbf{V}_g$ is the geostrophic velocity and the remaining symbols have their conventional meanings. The geostrophic approximation applies to those inviscid flow regimes for which the magnitude of the horizontal velocity acceleration, $|d\mathbf{V}/dt|$, is small in comparison to the Coriolis acceleration.

If we partition the horizontal velocity into its geostrophic and ageostrophic components, $\mathbf{V} = \mathbf{V}_g + \mathbf{V}_a$, the vector equation for inviscid horizontal motion may be written as a balance between the horizontal velocity acceleration and the ageostrophic motion $\mathbf{V}_a$

$$\frac{d\mathbf{V}}{dt} = -f\hat{k} \times \mathbf{V}_a. \qquad (2)$$

We may discuss the nature of the velocity accelerations which give rise to ageostrophic motions after expressing Eq. (1) in terms of its quasinatural coordinate components (see Haltiner and Martin, 1957). These equations are written

$$\hat{s}\left(\frac{dV}{dt} = -\frac{\partial\Phi}{\partial s} = -fV_{gn}\right), \qquad (3)$$

$$V\frac{d\hat{s}}{dt} = \hat{n}\frac{V^2}{R_t} = \hat{n}\left[-fV - \frac{\partial\Phi}{\partial n} = -f(V - V_{gs})\right], \qquad (4)$$

where $\hat{s}$ and $\hat{n}$ are the unit vectors in the direction along (tangential to) and normal to (to the left of) the horizontal velocity, respectively; s and n are the respective horizontal distances in the $\hat{s}$ and $\hat{n}$ directions; R_t is the radius of trajectory curvature; d/dt is the total time derivative; V is the total wind speed; and V_{gn} and V_{gs} are the components of $\mathbf{V}_g$ in the $\hat{n}$ and $\hat{s}$ directions, respectively.

Eqs. (3) and (4) partition the horizontal velocity acceleration into the wind-speed acceleration dV/dt in the along-flow $\hat{s}$ direction, and the centripetal acceleration, V^2/R_t, normal to $\hat{s}$. The speed acceleration of Eq. (3) is associated with a component of $\mathbf{V}$ across the height contours, which appears as gradients of Φ in the $\hat{s}$ direction. Eq. (4) gives the deviation from geostrophy resulting from curved trajectories.

There have been numerous applications of the equations of motion in describing velocity accelerations and ageostrophic motions in the vicinity of straight and curved jet stream currents. For example, Namias and Clapp (1949), Riehl (1955), and Uccel-

[1] The National Center for Atmospheric Research is sponsored by the National Science Foundation.

0022-4928/81/122642-11$06.75

lini and Johnson (1979) discussed the ageostrophic motions associated with speed-accelerating and -decelerating air parcels in the entrance and exit regions, respectively, of upper-tropospheric jet streaks. Newton and Persson (1962) diagnosed the ageostrophic velocities induced by centripetal accelerations at the sharply curved ($R_t \sim \pm 1000$ km) trough and ridge axes of a large-amplitude Rossby wave, finding ageostrophic motions of up to 60 m s^{-1} within a meandering jet stream current.

Fig. 1a presents a schematic representation of the cross-contour ageostrophic motions and divergence pattern associated with a straight jet streak. Fig. 1b illustrates the ageostrophic motions and the divergence of curved flow for a constant-velocity jet stream embedded within a stationary synoptic wave. In Fig. 1b, the wind speed is uniform along the flow and the jet is parallel to the height contours as is the case for a jet embedded within a stationary wave (see Newton and Omoto, 1965). The confluence and difluence of the height contours in the inflections are consistent with changes in curvature along the flow and contribute to the divergence.

Unfortunately, there are uncertainties in evaluating ageostrophic motions at jet stream levels of the atmosphere from conventional upper-air observations. These uncertainties arise from errors in rawinsonde instrumentation (see Danielsen, 1959, and Bruce *et al.*, 1977) and from the limited spatial and temporal resolution of the observing network. Specifically, the error of up to ±1°C in the vertically integrated temperature gives rise to 35 and 47 m height errors at 300 and 200 mb, respectively. An uncorrelated 30 m height error in two adjacent soundings 400 km apart [a height-gradient error of 30 m (400 km^{-1})] yields a geostrophic wind error of 15 m s^{-1} at 40°N, which equals ~25% of typical jet wind speeds. Errors in observed wind speed can exceed 20 m s^{-1} under high wind speed conditions when the measured balloon elevation angle becomes <10°. Rawinsonde wind direction errors of 10° coupled with uncertainties in geopotential height analysis due to the height error described above, make it difficult to evaluate the cross-contour ageostrophic wind component, as the angle between the observed wind velocity and the height contours rarely exceeds 30° during the most extreme cases of jet stream speed acceleration (deceleration). Estimates of the ageostrophic motions induced by centripetal acceleration are quite sensitive to errors in wind speed and to the uncertainties in specifying three-dimensional trajectory curvatures (taken along isentropic surfaces in the absence of diabatic processes) from the coarse temporal resolution of the 12 h synoptic observations. Finally, the spatial resolution of the synoptic observing network is too coarse for describing the mesoscale (~100 km) cross-jet wind shears found by research aircraft within jet streams (see Shapiro, 1976, 1978).

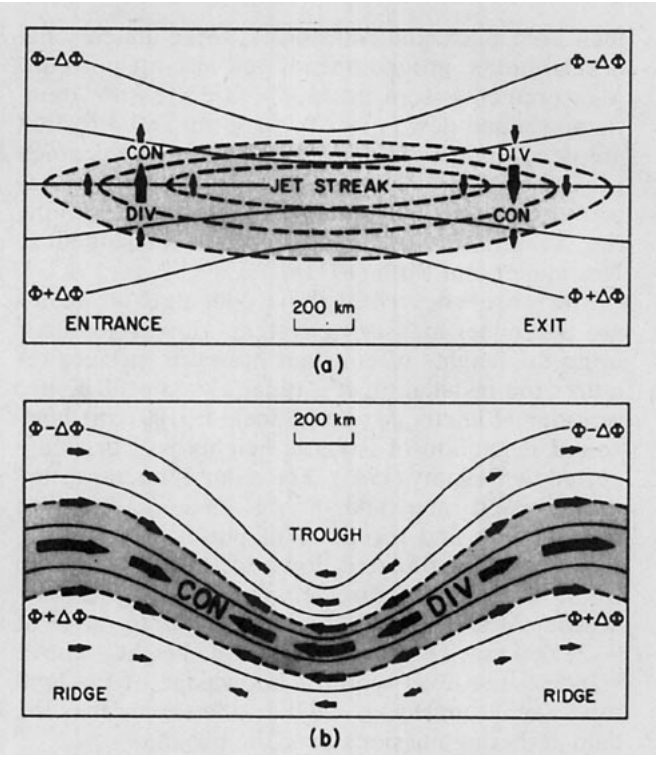

FIG. 1. Schematic representation of the ageostrophic motions (heavy arrows) and associated convergence (CON) and divergence (DIV) patterns in the vicinity of (a) straight jet-streak wind system, and (b) uniform jet within a stationary synoptic wave. Geopotential height contours, solid lines; isotachs, dashed lines; region of wind speed exceeding 50 m s^{-1}, shaded area.

In the present investigation, we combined the technologies of airborne radar altimetry and inertial-platform wind measurements to obtain a continuous mapping of the geostrophic and ageostrophic wind velocity components in the vicinity of a jet stream system near the tropopause. Section 2 of this article highlights the advantages of these observing techniques over the rawinsonde system. In Section 3, we apply the information derived from these research flights to the diagnosis of the horizontal velocity divergence and we assess the applicability of the geostrophic momentum approximation in the vicinity of sharply curved upper level jet streams.

2. Instrumentation

The North American Rockwell twin-jet Sabreliner, owned and operated by the National Center for Atmospheric Research (NCAR), provided the data which were recorded on magnetic tape with a time resolution of 1 s. A differential flow angle sensor measured airspeed, angle of attack, and sideslip, while a Litton LTN-51 inertial navigation system

measured pitch and roll angles, three-dimensional accelerations, ground speed, and aircraft position. Measurements were made of static pressure, temperature, and dew point. Wind speed and direction are derived quantities having an absolute accuracy of ~ 1 m s^{-1} and 1°, respectively, a significant improvement over the rawinsonde. Details describing the Sabreliner instrumentation are presented in Newcomer and Ruth (1973).

The sensors described above constitute the standard Sabreliner measuring system. However, measuring the heights of constant pressure surfaces requires the installation of a radar altimeter. The use of radar altimetry for small-scale (~ 100 km) horizontal resolution of isobaric heights was first suggested by Bellamy (1945). The radar altimeter measures elapsed time (and, hence, distance) between transmission and reception of pulses of radio-frequency energy directed down to, and reflected up from, the earth's surface. We used a Stewart-Warner Model APN-159 with an altitude range of 0–21 000 m. To obtain pressure heights above standard sea level requires knowledge of the land topography, unless, as we did, one simply flies the data-gathering missions over the ocean.

An accurate measurement of static pressure is required, for it is from static pressure that the U.S. Standard Atmosphere height is determined. The difference between this "standard" height and the radar altitude is the D-value (see Bellamy, 1945). The D-value method eliminates the influence of small deviations from constant pressure on the measured height field; these deviations are caused by ± 1 mb variations in pressure as the autopilot servos strive to maintain a nominal constant-pressure altitude.

Errors in both the radar altitude and the static pressure contribute to errors in the D-value. We determined that the rms error in D-value at 300 mb is ± 6.0 m, which includes some unknown amount of high-frequency "noise." Since high-frequency (>0.02 Hz) information was not required for our purposes, the D-values were filtered to further reduce the 6 m rms error which represents a substantial improvement over the ~ 40 m error of the rawinsonde. Details on the calculation of the D-value, altimeter error analysis, and the technical specifications of the APN-159 altimeter are presented in Brown *et al.* (1981).

In summary, the advantages of these airborne observing techniques over the rawinsonde network lie in both the greater accuracy and the enhanced spatial resolution of the measurements.

3. Case study: 2 March 1979

At 2100 GMT 1 March 1979, the NCAR Sabreliner departed from Jefferson County Airport, Broomfield, Colorado, to begin the first of two research missions aimed at documenting the meteoro-

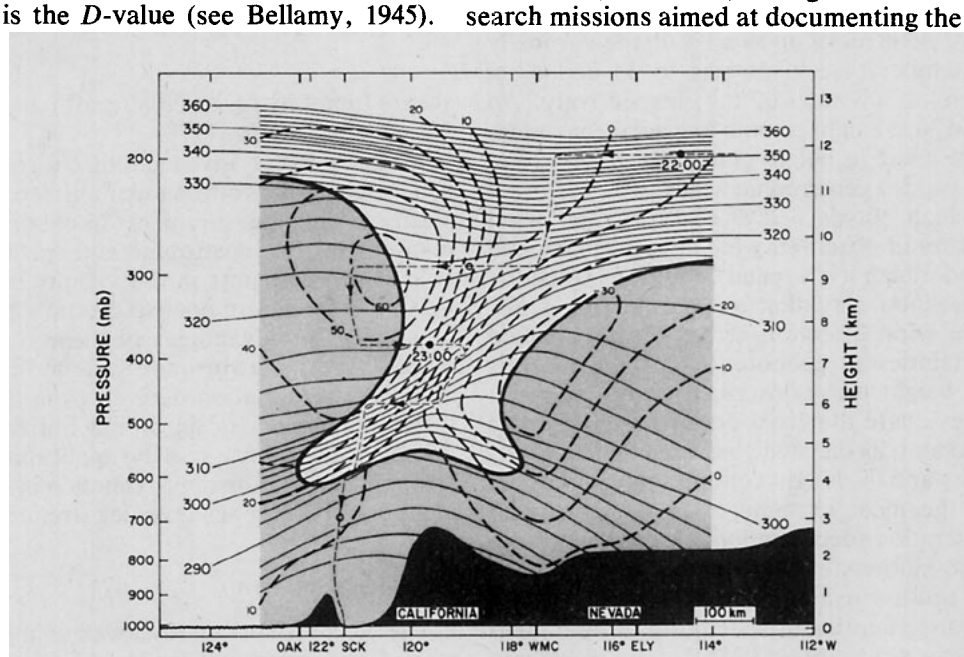

FIG. 2. Cross section of potential temperature (K, solid lines), and wind speed component normal to the cross section (m s^{-1}), along the line $\overline{AA'}$ of Fig. 3 at 0000 GMT 2 March 1979. Sabreliner flight track, thin dashed lines. Tropopause as defined by the 10^{-7} s^{-1} K mb^{-1} isopleth of potential vorticity, heavy solid line. Shaded area, the troposphere. NWS balloon soundings from Oakland, California (OAK), Winnemucca, Nevada (WMC), and Ely, Nevada (ELY), aided in this analysis.

logical characteristics of a jet stream flowing from north to south near the Pacific coast of California. The first flight provided meteorological data which, when combined with the 0000 GMT 2 March 1979 synoptic upper air observations from Oakland, California (OAK), Winnemucca, Nevada (WMC), and Ely, Nevada (ELY), revealed the vertical structure of this upper level jet front system. The resulting cross-section analysis (Fig. 2), prepared along the projection line $\overline{AA}'$ of Fig. 3, reveals the presence of a northerly jet stream core in excess of 60 m s^{-1} at 300 mb over Stockton, California (SCK), with its associated front between 400 and 700 mb. The 300 mb wind vectors and height analysis for 0000 GMT 2 March 1979 (Fig. 3) show that Fig. 2 cuts across the sharp upper trough over the southern Pacific coastal area of the United States.

After refueling at Stockton, the Sabreliner commenced its second mission with the objective of mapping the observed, geostrophic and ageostrophic wind fields of this jet-stream system over the Pacific Ocean south of San Diego, California. Fig. 4 presents the flight track and wind speed analysis for the segment of the second flight between 0200 and 0430 GMT 2 March 1979 at 285 mb. The second flight was a zigzag track in the downwind direction (southward), with the return leg northward and a landing at San Diego. This flight provided a data base having a high spatial resolution from which wind velocity and D-value analyses were derived. The observations from both research flights were space-time adjusted to 0300 GMT 2 March 1979 so as to account for the 25 m s^{-1} east-southeastward propagation of the jet during the 5 h time span of the two flights. The propagation velocity was determined from spatially adjusting the nonsimultaneous flight leg data taken from the two research flights. The wind speed analysis (Fig. 4) reveals a >70 m s^{-1} jet core on the Pacific coast. Parcels decelerated as they left the jet core southwest of San Diego.

Fig. 5 presents an example of the wind speed and D-value observations used in the analysis. These data, taken along the flight segment $\overline{CC}'$ of Fig. 4, were filtered along with data from other flight segments to remove the ≤10 km wind and D-value fluctuations prior to the preparation of the mesoscale (~100 km) depiction of the jet stream characteristics. Fig. 5 reveals a typical wind speed profile across a jet axis as found in earlier aircraft investigations by Shapiro (1976, 1978). The D-value trace shows a monotonic decrease in the height of the 285 mb surface along the track, with a suggestion of greater slope near the jet core.

The analysis of the 285 mb D-value data (Fig. 6) shows curved height contours in the vicinity of the exit region, where the jet approaches the trough axis. The angle deviation between the height contours and the observed wind direction is such that the observed wind is directed across the height contours toward greater heights, implying deceleration as air parcels leave the jet streak. It should be noted that the observed wind speed *decreases* in the downwind direction along the jet axis (Fig. 4), whereas the geostrophic wind speed *increases* along the jet axis, consistent with the cyclonically curved motions near the trough axis in Fig. 3.

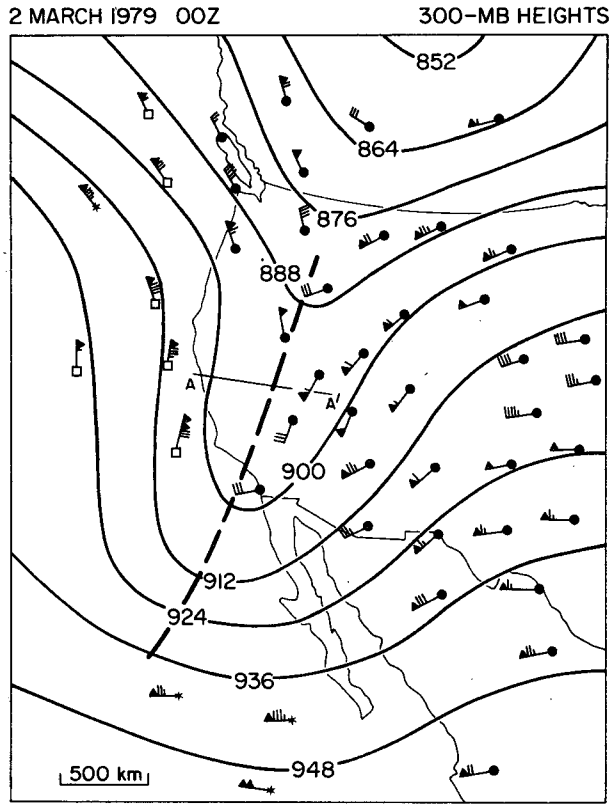

FIG. 3. NMC 300 mb height analysis at 0000 GMT 2 March 1979. Heights (10 m, solid lines), wind speed (flag, 25 m s^{-1}; barb, 5 m s^{-1}; half barb, 2.5 m s^{-1}), rawinsonde winds (circle), aircraft winds (square), cloud motion winds (star). Trough axis, heavy dashed line. Line $\overline{AA}'$ is the cross section projection line for Fig. 2.

Fig. 7 presents the speed and direction analysis of the ageostrophic velocity, which was determined from the observed wind velocity (Fig. 4) and D-value (Fig. 6) analyses. The results show that the ageostrophic motions are southeasterly against the northwesterly observed wind and exhibit difluence in the exit region of the jet. The speed of the ageostrophic wind is >80 m s^{-1} near the trough axis and diminishes upstream along the jet axis as the wind becomes less ageostrophic near the jet maximum of Fig. 4. In addition, we calculated the component of the ageostrophic wind directed across the D-value height contours (Fig. 6), and the results are presented in Fig. 8. Here, the cross-contour ageostrophic motions are greatest in the vicinity of the jet axis, ex-

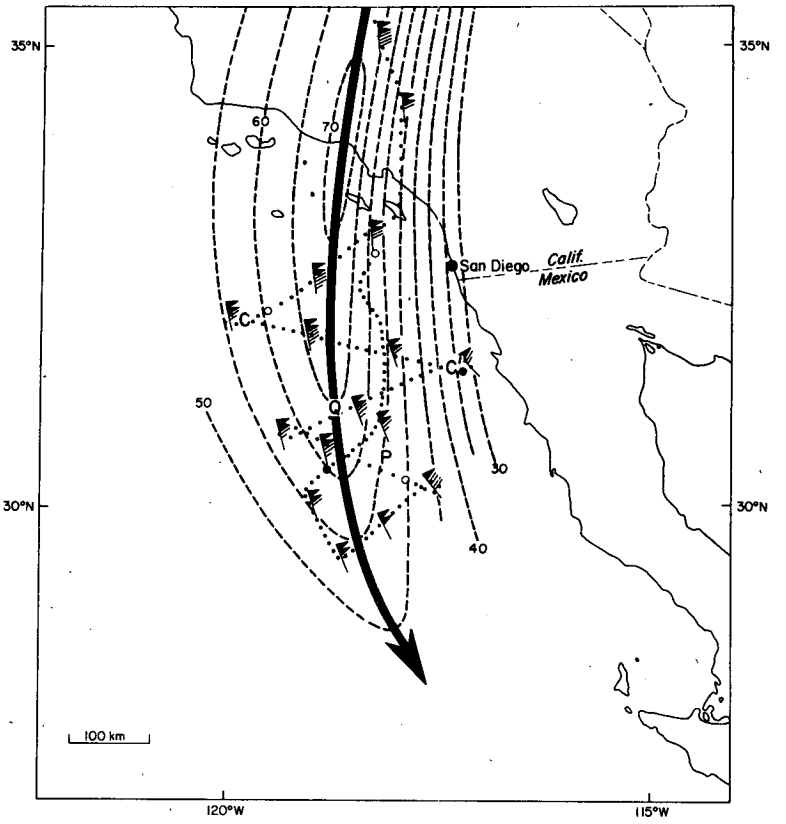

FIG. 4. Wind speed (m s^{-1}) analysis at 285 mb for Sabreliner flight data taken between 0200 and 0430 GMT 2 March 1979. Wind flags and barbs, same as Fig. 3. Flight track, dotted line with hourly (solid circle) and half hourly (open circle) time hacks. Heavy solid line with arrow marks the axis of jet stream.

ceeding -22 m s^{-1} at the southernmost portion of the research flight.

The magnitude of the wind speed and centripetal acceleration terms of Eqs. (3) and (4), respectively,

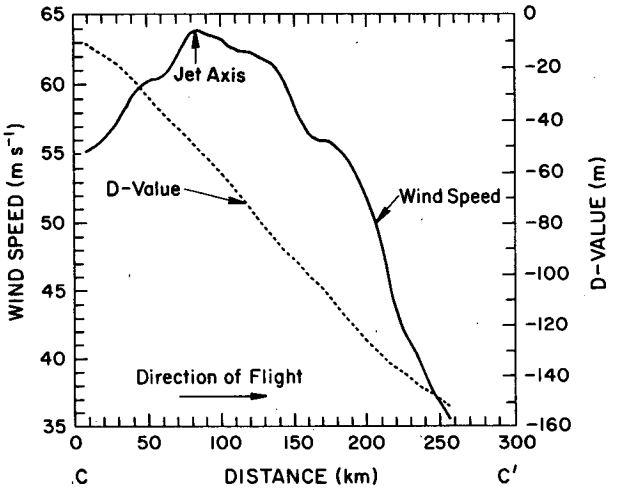

FIG. 5. Component of observed wind speed (m s^{-1}) parallel to the D-value height contours and D-value (m) profiles along the line $\overline{CC'}$ of Figs. 4 and 6.

were calculated over the flight region after we obtained the along- and cross-wind components (V_{gs} and V_{gn}, respectively) of the geostrophic velocity $\mathbf{V}_g$ from the D-value height analysis of Fig. 6. Fig. 9a illustrates the momentum losses ($dV/dt < 0$) associated with the decelerating air parcels as they travel toward higher heights in the jet exit region. Fig. 9b shows the effect of the cyclonic trajectory motions ($R_t > 0$), which give rise to large along-wind ageostrophic motions and associated centripetal acceleration, where the exit region of the jet enters the trough axis (Fig. 4). The results presented within Figs. 9a and 9b indicate that both components of the velocity acceleration are of comparable magnitude to the Coriolis acceleration, $|f\hat{k} \times \mathbf{V}|$, which equals 44×10^{-4} m s^{-2} at 30°N for $V = 60$ m s^{-1}. We conclude that *the jet stream motions were not in geostrophic balance with the geopotential height gradient.*

The horizontal velocity divergence $\nabla \cdot \mathbf{V}$ may be calculated either from the observed wind field or from the ageostrophic motions. For the present study, we selected the ageostrophic form. The horizontal velocity divergence is given by

$$\nabla \cdot \mathbf{V} = \nabla \cdot \mathbf{V}_g + \nabla \cdot \mathbf{V}_a, \qquad (5)$$

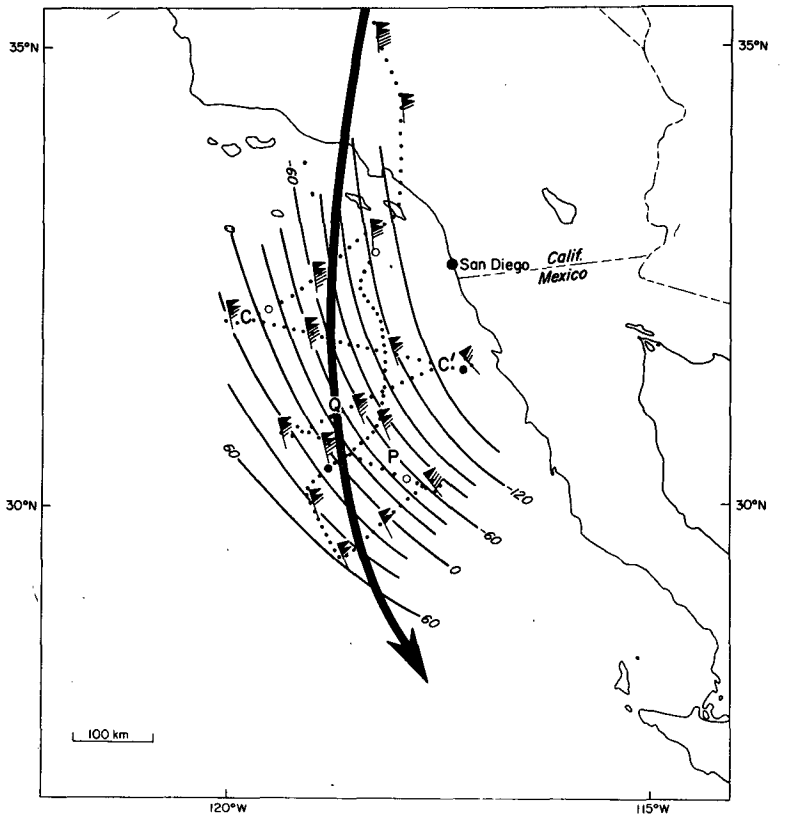

FIG. 6. D-value height analysis (m) for Fig. 4 jet stream. Flags, barbs, and heavy solid line arrow, same as Fig. 4.

where

$$\mathbf{V}_g = \frac{\hat{k}}{f} \times \nabla\Phi, \tag{6}$$

which when entered into Eq. (5) gives

$$\nabla\cdot\mathbf{V} = \nabla\cdot\mathbf{V}_a - \frac{v_g}{f}\beta, \tag{7}$$

where v_g is the meridional component of $\mathbf{V}_g$ and $\beta = \partial f/\partial y$. The first term on the right-hand side of Eq. (7) is the divergence of the ageostrophic wind and the second term is the divergence of the geostrophic wind arising from β.

Expanding the horizontal gradient operator with respect to the ageostrophic motions we obtain from Eq. (7)

$$\nabla\cdot\mathbf{V} = \frac{\partial V_a}{\partial s'} - V_a\left(\frac{\partial\psi'}{\partial n'}\right) - \frac{v_g}{f}\beta, \tag{8}$$

where V_a is the magnitude of $\mathbf{V}_a$, ψ' is the meteorological wind direction angle of $\mathbf{V}_a$, and s' and n' are the distances along $\mathbf{V}_a$ and normal and to the left of $\mathbf{V}_a$, respectively.

Point P of Figs. 4, 6, 7, 8, and 9 was chosen to evaluate the contributions of the individual terms of Eq. (8) to the divergence. This point is situated within the cyclonic shear portion of the region of the jet. From the ageostrophic wind velocity analysis (Fig. 7), the terms of Eq. (8) were calculated to be

$$\frac{\partial V_a}{\partial s'} = -1.8 \times 10^{-4}\ \mathrm{s}^{-1},$$

$$-V_a\left(\frac{\partial\psi'}{\partial n'}\right) = 1.0 \times 10^{-4}\ \mathrm{s}^{-1},$$

$$-\frac{v_g}{f}\beta = -0.5 \times 10^{-4}\ \mathrm{s}^{-1}, \tag{9}$$

which when summed give a divergence of

$$\nabla\cdot\mathbf{V} = -1.3 \times 10^{-4}\ \mathrm{s}^{-1}. \tag{10}$$

The total divergence is less than zero (convergence) because of the dominance of the speed convergence of the ageostrophic velocity, $\partial V_a/\partial s' < 0$, and the β term. This finding of convergence in the left-front quadrant of a jet streak is discussed below.

The diagnosis and the analytical and numerical modeling of secondary circulations in the vicinity of upper jet-front systems have been discussed by Namias and Clapp (1949), Riehl (1955), Sawyer (1956), Eliassen (1962), Hoskins and Bretherton

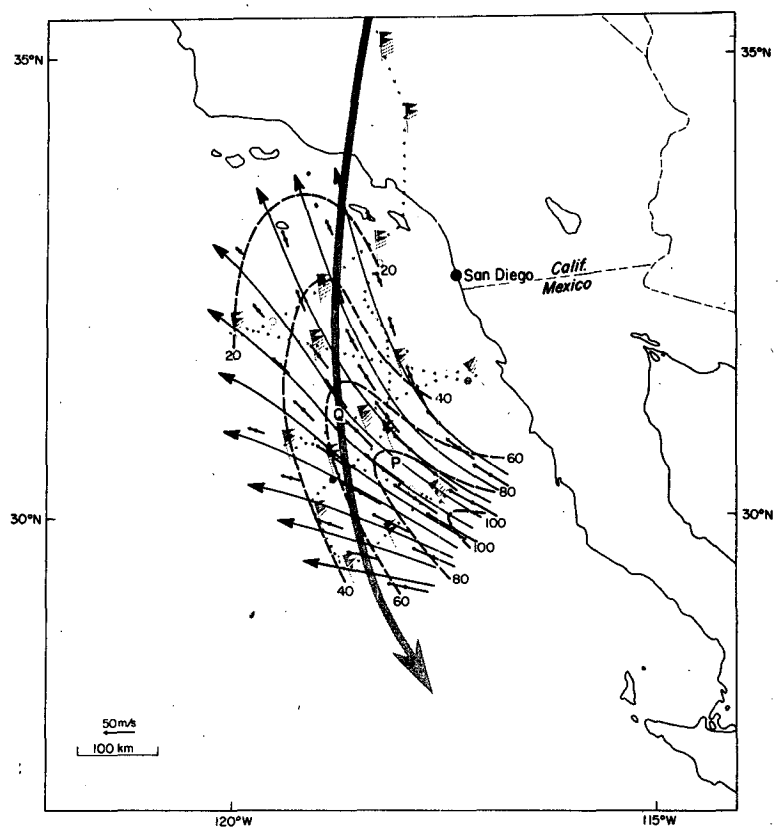

FIG. 7. Ageostrophic wind velocity as determined from the Fig. 4 observed wind velocity and Fig. 6 geostrophic height contour analyses. Ageostrophic wind speed (m s^{-1}, dashed lines) and wind direction streamlines (solid lines).

(1972), Uccellini and Johnson (1979), Gidel and Shapiro (1979), and Shapiro (1981). These studies have the common assumptions that (1) the ratio of the length of these systems to their width is sufficiently large that the ageostrophic circulations are confined to the cross-jet plane, (2) the along-jet wind component is approximately geostrophic, and (3) the horizontal velocity acceleration is closely approximated by the acceleration of the geostrophic velocity (the geostrophic momentum approximation). These assumptions and approximations are most suited to near-straight jet-front systems such as the one illustrated in Fig. 1a. Many cases of upper jet-front systems do evolve under these conditions. But in other cases, such as the jet-streak impulses which form and propagate through the Rossby wave regime of middle and high latitudes, the validity of applying the above assumptions is open to question.

The present case study is an example of a jet-streak impulse situated within a sharply curved ($|R_t| \leq 1000$ km) upper level, synoptic-scale wave. We shall use this example for the diagnosis of the application of the above physical and theoretical approximations to jet-front systems embedded within meandering large-amplitude flows. We shall consider both the extent to which the divergence is confined to the cross-jet plane and the degree to which the example presented satisfies the geostrophic momentum approximation.

The cross-contour ageostrophic wind component v_a as calculated from the wind velocity and D-value height analyses of Figs. 4 and 6, respectively, was shown in Fig. 8. The contribution of v_a to the horizontal velocity divergence at the point P of Fig. 8 is

$$\frac{\partial v_a}{\partial y} = 1.8 \times 10^{-4}\ \mathrm{s}^{-1}, \tag{11}$$

where y is normal to and to the left of the geostrophic motions. A comparison of Eq. (11) with the values presented in Eqs. (9) and (10) reveals that the divergence is *not* given by the cross-contour component of the ageostrophic wind in the present case. Here, the ageostrophic motions induced by the centripetal acceleration give rise to a substantial (in this case compensating) contribution to the divergence. The effects of curvature on the divergence give a net

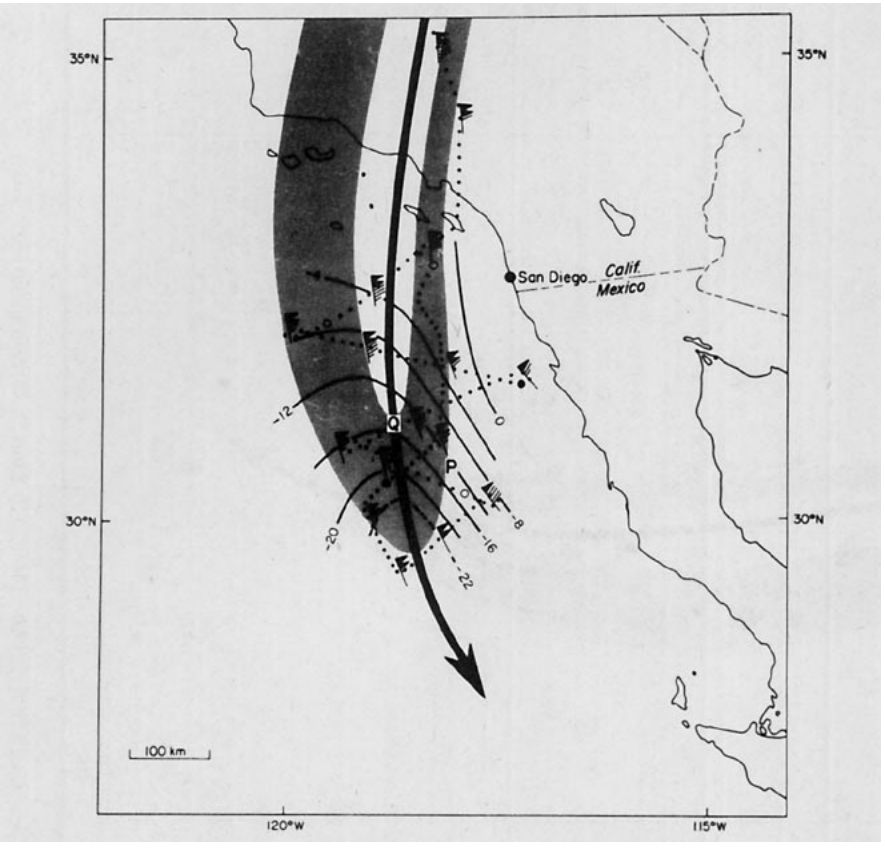

FIG. 8. Magnitude of the cross-height-contour component of the ageostrophic velocity (m s^{-1}). Shaded area is the 55 to 65 m s^{-1} speed region of Fig. 4. Heavy solid arrow, flags, barbs, and flight track, same as Fig. 4.

convergence in the left-front quadrant of the jet streak, in contrast to the classical *divergence* found in this region for straight jet streaks (Fig. 1a). Furthermore, the ageostrophic velocity in the vicinity of point P (Fig. 7) bears only a slight resemblance to the classical jet-streak ageostrophic motions (Fig. 1a) because of the contribution by the curvature. The present example is one in which the effects of both straight jet-streak dynamics (Fig. 1a) and the curvature effects of wave dynamics (Fig. 1b) are contributing to the ageostrophic motions and divergence within the jet.

The geostrophic momentum (GM) approximation was introduced by Eliassen (1948) and is written

$$\frac{d\mathbf{V}}{dt} = \frac{d\mathbf{V}_g}{dt} + \frac{d\mathbf{V}_a}{dt} \approx \frac{d\mathbf{V}_g}{dt} = -f\hat{k} \times \mathbf{V}_a, \quad (12)$$

where the substantial time derivative expands as

$$\frac{d}{dt} = \frac{\partial}{\partial t} + (\mathbf{V}_g + \mathbf{V}_a)\cdot\nabla + \omega\frac{\partial}{\partial p}, \quad (13)$$

where ω is the pressure coordinate vertical component of motion. The GM approximation omits the acceleration of the ageostrophic motion while retaining the horizontal and vertical ageostrophic advections in the substantial derivative.

The GM form of the equation of motion in quasi-natural coordinates is

$$\hat{s}\left(\frac{dV_g}{dt} = -\frac{\partial\Phi}{\partial s} = -fV_{gn}\right) \quad (14)$$

$$V_g\frac{d\hat{s}}{dt} = \hat{n}\frac{V_g V}{R_t} = \hat{n}\left[-fV - \frac{\partial\Phi}{\partial n} = -f(V - V_{gs})\right] \quad (15)$$

From Eqs. (3), (4), (14) and (15) we find that the GM approximation neglects the ageostrophic speed acceleration, dV_a/dt, and a portion of the centripetal acceleration, $V_a V/R_t$.

Point Q of Figs. 4, 6, 8 and 9 was selected to calculate the differences between the observed velocity acceleration components of Eqs. (3) and (4) and their GM-approximated forms in Eqs. (14) and (15). Point Q lies on the jet axis in the center of the

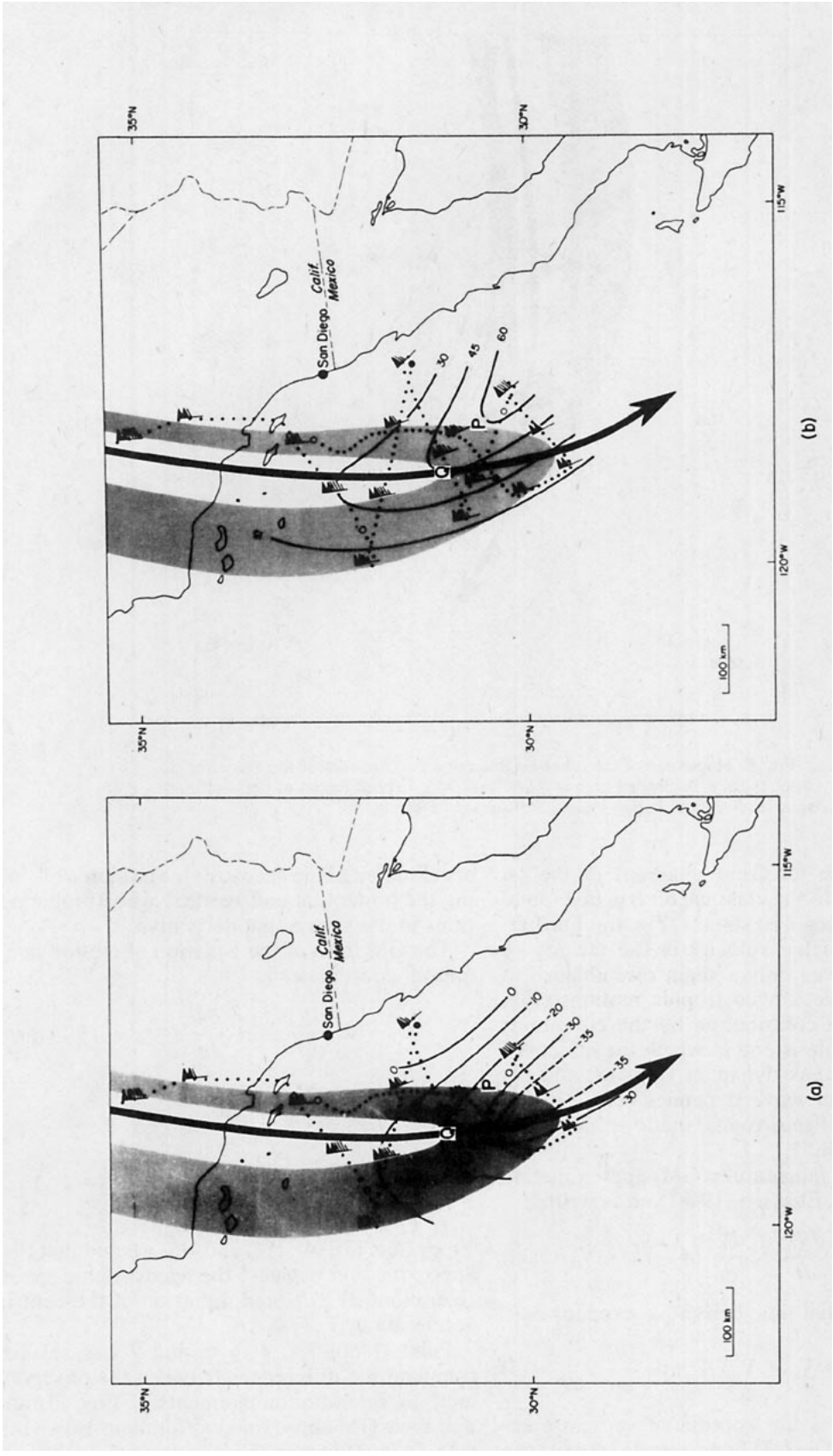

FIG. 9. Components of the observed horizontal velocity acceleration, dV/dt: (a) speed acceleration, $dV/dt = -fV_{gn}(10^{-4}\ \mathrm{m\,s^{-2}})$; (b) centripetal acceleration $V^2/R_t = -f(V - V_{ga})(10^{-4}\ \mathrm{m\ s^{-2}})$. Shaded area, flags, barbs, flight track, and heavy solid arrow, same as Fig. 8.

observations in a region of maximum speed and centripetal acceleration (see Fig. 9). The GM speed acceleration, dV_g/dt, was calculated assuming that (1) the vertical advection, $\omega\partial V_g/\partial p$, was negligible at the level of maximum wind velocity where air motions are nearly horizontal ($\omega \approx 0$) and vertical gradients of V_g are negligible; and (2) the local tendency, $\partial V_g/\partial t$, is given by its phase velocity advection, $-\mathbf{c}\cdot\nabla V_g$, where $\mathbf{c}$ is the east-southeastward propagation velocity of the jet system. The GM centripetal acceleration, VV_g/R_t, was calculated by solving for the radius of trajectory curvature R_t from the values of V and V^2/R_t from Figs. 4 and 9, respectively. The tabulation of the observed and GM velocity acceleration components (Table 1) reveals significant differences between them. From Table 1, we find that the observed and GM speed accelerations are of opposite sign, as the GM approximation gives a positive *acceleration* ($dV_g/dt > 0$) where the observed wind speed is *decelerating* ($dV/dt < 0$). From the GM speed acceleration alone, one would deduce that the cross-contour motions should be directed toward *lower* heights instead of toward *higher* heights, as is the case in Figs. 6 and 8. The difference (observed minus GM) is the acceleration of the ageostrophic wind speed, dV_a/dt, which dominates the GM contribution to the observed speed acceleration. The observed and GM centripetal accelerations are of the same sign, with the GM component being larger since $V_g \gg V$ in the cyclonically curved, jet exit region. Table 1 also presents the difference (observed minus GM) to illustrate the contributions by the ageostrophic terms neglected by the GM approximation.

TABLE 1. Components of the observed and geostrophic momentum velocity acceleration as evaluated at the point Q of Figs. 4, 6, 8 and 9.

	Speed acceleration	Centripetal acceleration
Observed acceleration	$\frac{dV}{dt} = -2.0 \times 10^{-3}$ m s^{-2}	$\frac{V^2}{R_t} = 4.5 \times 10^{-3}$ m s^{-2}
GM acceleration	$\frac{dV_g}{dt} = 9 \times 10^{-3}$ m s^{-2}	$\frac{VV_g}{R_t} = 9 \times 10^{-3}$ m s^{-2}
Difference (obs. − GM)	$\frac{dV_a}{dt} = -11 \times 10^{-3}$ m s^{-2}	$\frac{VV_a}{R_t} = -4.5 \times 10^{-3}$ m s^{-2}

4. Summary and suggestions for future research

In the present article, we have shown the results of combining the technologies of airborne radar altimetry and inertial wind velocity measurements to obtain a continuous horizontal mapping of geostrophic and ageostrophic wind velocity components in the vicinity of a jet stream system. The results revealed the characteristics of the observed, geostrophic and ageostrophic wind velocities in the exit region of a jet streak embedded within an area of cyclonic trajectory curvature.

Calculations of the horizontal velocity divergence from the ageostrophic velocity illustrated *the importance of centripetal-acceleration-induced ageostrophic motions* (Fig. 1b) *in modifying the classical divergence pattern in the exit region of a jet streak* (Fig. 1a). An examination of the individual components of the total velocity acceleration revealed that the geostrophic momentum approximation is unsuitable where the exit region of the jet entered into the trough of a synoptic wave. It was there that the accelerations of the geostrophic velocity and ageostrophic velocity were found to have comparable magnitudes and to be of opposite sign. *These results raise the question of whether straight jet-streak dynamics and the geostrophic momentum approximation apply to cases in which jet-streak systems are embedded within synoptic wave regimes.*

In future experimentation, we intend to measure ageostrophic motions over irregular, but not mountainous, topography in the regions of conventional upper air data coverage. Given high-resolution (1 km) digital topography along with comparable accuracy in the location of the research aircraft, the variation in the height of the underlying earth's surface may be removed from the radar altimeter measurements. Through these measurements, intercomparisons may be made between the ageostrophic motions observed by research aircraft and those analyzed and predicted by numerical weather prediction methods.

Another application of this technology is to observe the response of jet streams to the ageostrophic motions forced by mesoscale convective complexes (see Ninomiya, 1971; Fritch and Maddox, 1981).

Acknowledgments. The authors express thanks to Drs. Fred Sanders and Daniel Keyser for their helpful comments on this research.

REFERENCES

Bellamy, J. C., 1945: The use of pressure altitude and altimeter corrections in meteorology. *J. Meteor.*, **2**, 1–79.

Brown, E. N., M. A. Shapiro, P. J. Kennedy and C. A. Friehe, 1981: The application of airborne radar altimetry to the measurement of height and slope of isobaric surfaces. *J. Appl. Meteor.*, **20**, 1070–1075.

Bruce, R. E., L. D. Duncan and J. H. Pierluissi, 1977: Experimental study of the relationship between radiosonde temperatures and satellite-derived temperatures. *Mon. Wea. Rev.*, **105**, 493–496.

Danielsen, E. F., 1959: The laminar structure of the atmosphere and its relation to the concept of the tropopause. *Arch. Meteor. Geophys. Bioklim.*, **A11**, 293–332.

Eliassen, A., 1948: The quasi-static equations of motion. *Geofys. Publ.*, **17**, No. 3.

——, 1962: On the vertical circulation in frontal zones. V. Bjerknes Memorial Volume, *Geofys. Publ.*, **24,** 147–160.

Fritch, J. M., and R. A. Maddox, 1981: Convectively driven mesoscale weather systems aloft. Part I: Observations. *J. Appl. Meteor.*, **20,** 9–19.

Gidel, L. T., and M. A. Shapiro, 1979: The role of clear air turbulence in the production of potential vorticity in the vicinity of upper tropospheric jet stream-frontal systems. *J. Atmos. Sci.*, **36,** 2125–2138.

Haltiner, G. J., and F. L. Martin, 1957: *Dynamical and Physical Meteorology*. McGraw-Hill, 470 pp.

Hoskins, B. J., and F. P. Bretherton, 1972: Atmospheric frontogenesis models: Mathematical formulation and solution. *J. Atmos. Sci.*, **29,** 11–37.

Namias, J., and P. F. Clapp, 1949: Confluence theory of the high tropospheric jet stream. *J. Meteor.*, **6,** 330–336.

Newcomer, L. E., and R. Ruth, 1973: The NCAR Sabreliner. *Atmospheric Technology,* **1,** National Center for Atmospheric Research, 28–30.

Newton, C. W., and A. V. Persson, 1962: Structural characteristics of the subtropical jet stream and certain lower stratospheric wind systems. *Tellus*, **14,** 221–241.

——, and Yukio Omoto, 1965: Energy relation near jet stream, and associated wave-amplitude relations. *Tellus*, **14,** 449–462.

Ninomiya, K., 1971: Mesoscale modification of synoptic situations from thunderstorm development as revealed by ATS III and aerological data. *J. Appl. Meteor.*, **10,** 1103–1121.

Riehl, H., 1955: *The Jet Stream. Meteor. Monogr.*, No. 7, Amer. Meteor. Soc., 176 pp.

Sawyer, J. S., 1956: The vertical circulation at meteorological fronts and its relationship to frontogenesis. *Proc. Roy. Soc. London*, **A234,** 346–362.

Shapiro, M. A., 1976: The role of turbulent heat flux in the generation of potential vorticity in the vicinity of upper-level jet stream systems. *Mon. Wea. Rev.*, **104,** 892–900.

——, 1978: Further evidence of the mesoscale and turbulent structure of upper-level jet stream-frontal zone systems. *Mon. Wea. Rev.*, **106,** 1100–1111.

——, 1981: Frontogenesis and geostrophically forced secondary circulations in the vicinity of jet stream-frontal zone systems. *J. Atmos. Sci.*, **38,** 954–973.

Uccellini, L. W., and D. R. Johnson, 1979: The coupling of upper and lower tropospheric jet streaks and implications for the development of severe convective storms. *Mon. Wea. Rev.*, **107,** 682–703.